Journal of Power Sources 187 (2009) 371–377

Contents lists available at ScienceDirect

Journal of Power Sources

journal homepage: www.elsevier.com/locate/jpowsour

Characterization of perovskite-type cathode, $La_{0.75}Sr_{0.25}$ $Mn_{0.95-x}Co_x$ $Ni_{0.05}O_{3+\delta}$ ($0.1 \leq x \leq 0.3$), for intermediate-temperature solid oxide fuel cells

Ravindra K. Gupta, Ik-Jin Choi, Yong-Soo Cho*, Hong-Lim Lee, Sang-Hoon Hyun

Department of Materials Science and Engineering, Yonsei University, Seoul 120-749, Republic of Korea

ARTICLE INFO

Article history:
Received 16 May 2008
Received in revised form
15 September 2008
Accepted 22 October 2008
Available online 21 November 2008

Keywords:
Doped $LaMnO_3$
Cathode
Structure
Thermal property
Electrical conductivity

ABSTRACT

Phase evolution, structure, thermal property, morphology, electrical property and reactivity of a perovskite-type cathode system, $La_{0.75}Sr_{0.25}$ $Mn_{0.95-x}Co_xNi_{0.05}O_{3+\delta}$ ($0.1 \leq x \leq 0.3$), are reported. The samples are synthesized using metal acetates by the Pechini method. A perovskite-type phase is formed after calcination at ~700 °C and a rhombohedral symmetry of R – 3*c* space group is stabilized at ~1100 °C. An increase in *x* decreases the unit cell volume linearly, accompanying with a linear decrease in bond lengths and tilt angle. The differential thermal analysis suggests the phase stabilization for a temperature range, 50–1100 °C. The thermo-gravimetric, thermal expansion, and electrical and ionic conductivities studies suggest presence of a Jahn–Teller transition at ~260–290 °C. The samples with $x = 0.1$ mol exhibit electrical conductivity of ~55 S cm^{-1} at ~600 °C, activation energy of ~0.13 eV, coefficient of thermal expansion of ~12×10^6 °C^{-1}, crystallite size of ~45 nm, Brunauer–Emmett–Teller (BET) surface area of 1.26 m^2 g^{-1} and average particle size of ~0.9 μm. A fairly high ionic conductivity, 5–9 × 10^{-2} S cm^{-1} makes the sample with $x = 0.1$ mole suitable for intermediate-temperature solid oxide fuel cell cathode applications. The experimental results are discussed with the help of the defect models proposed for $La_{1-x}Sr_xMnO_{3+\delta}$.

© 2008 Elsevier B.V. All rights reserved.

1. Introduction

Intermediate-temperature solid oxide fuel cells (IT-SOFCs) operating at 600–800 °C, are the most efficient way of generating electricity due to internal reforming of hydrocarbon fuels, high quality by-product heat for co-generation, low level of pollutants, high energy conversion efficiency and electrical power of multi-mega Watt. The low temperature operation reduces not only the challenges regarding the materials' compatibility but also the manufacturing cost by using relatively inexpensive metal components for inter-connector, current collector, heat exchanger and structure components. A reduction in unit cell thickness to micro-level also enhances thermal shock resistance and reduces thermal mass, consequently reducing the start up and turn off time of the device [1–3]. It requires a new highly catalytic active cathode in place of the traditionally applied cathode, $La_{1-x}Sr_xMnO_{3+\delta}$ (LSM, $x = 0.2$–0.3 mol), which exhibits a low oxygen self-diffusion coefficient (D^*) ~10^{-14} cm^2 s^{-1} at 900 °C. A number of cathodes, derived from the highly catalytic active Sr^{2+} doped $LaM'O_{3-\delta}$ (M′ = Co, Fe or Ni), has already been investigated in the past [2]. Some of the cathodes are, $La_{0.6}Sr_{0.4}$ $Co_{0.2}Fe_{0.8}O_3$ (LSCF) [4], $La_{0.8}Sr_{0.2}$ $Co_{0.9}Ni_{0.1}O_3$ (LSCN) [5], $La_{0.8}Sr_{0.2}$ $Fe_{0.9}Ni_{0.1}O_3$ (LSFN) [5], $(La_{0.8}Sr_{0.2})_{0.98}$ $Fe_{0.98}Cu_{0.02}O_3$ (LSFCu) [6], $La_{0.6}Sr_{0.4}$ $Co_{0.6}Ga_{0.4}O_3$ (LSCG) [7] and $Ba_{0.5}Sr_{0.5}$ $Co_{0.8}Fe_{0.2}O_3$ (BSCF) [8]. The LSCF exhibited several superior properties, namely high electrical conductivity (σ) ~330 S cm^{-1} at 600 °C, high D^* ~10^{-7} cm^2 s^{-1} at 800 °C, theoretical density (ρ_{th}) ~6.36 g cm^{-3}, relative density (ρ) ~89%, rhombohedral structure and no reaction with electrolytes [2,4,9]. However, the coefficient of thermal expansion (α) ~15.3×10^{-6} °C^{-1} of LSCF was higher than those of IT-SOFC electrolytes, e.g. scandia-stabilized zirconia (ScSZ), $Ce_{0.9}Gd_{0.1}O_{1.95}$ (CGO) and $La_{0.9}Sr_{0.1}$ $Ga_{0.8}Mg_{0.2}O_3$ (LSGM) [2]. An attempt was also made to increase the catalytic activity of LSM (Sr^{2+} content = 0.16, 0.4 or 0.5 mol) by doping Fe^{2+}, Co^{2+} or Ni^{2+} (≤0.4 mol) in the Mn-site [9–13]. The doping decreased the electrical conductivity of LSM; however, the coefficient of thermal expansion was increased for Co^{2+}-doping, and left invariant for Fe^{2+}- and Ni^{2+}-doping. The doping also largely reduced the interfacial polarization resistance between the doped LSM and an electrolyte, and consequently enhanced the power density [12,13]. Carter et al. [9] noticed that a co-doping of Co^{2+} (0.12 mol) and Ni^{2+} (0.4 mol) is very effective in increasing the catalytic activity of $La_{0.5}Sr_{0.5}MnO_3$, as the D^* of LSM was enhanced approximately 6 orders of magnitude at 900 °C due to formation of additional oxygen vacancies.

In the present paper, an effect of co-doping of Co^{2+} and Ni^{2+} in Mn-site of a commonly used composition of the LSM, $La_{0.75}Sr_{0.25}$ $MnO_{3+\delta}$ is reported for IT-SOFC application via studying the phase evolution, structure, oxygen stoichiometry, thermal expansion,

* Corresponding author. Tel.: +82 2 2123 5848; fax: +82 2 365 5882.
E-mail address: ycho@yonsei.ac.kr (Y.-S. Cho).

0378-7753/$ – see front matter © 2008 Elsevier B.V. All rights reserved.
doi:10.1016/j.jpowsour.2008.10.136

morphology, electrical properties and reactivity. The Ni^{2+} concentration is fixed to 0.05 mole and Co^{2+} content is varied from 0.1 to 0.3 mol for increasing ionic conductivity and maintaining a thermal expansion coefficient comparable to those of IT-SOFC electrolytes [2,3]. The experimental results are discussed in the light of defect models proposed for LSM.

2. Experimental

$La_{0.75}Sr_{0.25}Mn_{0.95-x}Co_xNi_{0.05}O_{3+\delta}$ ($0.1 \le x \le 0.3$) is prepared by the Pechini method [14] using commercially available Aldrich chemicals, lanthanum (III) acetate hydrate (99.9%), strontium acetate hydrate (97%), manganese (II) acetate tetrahydrate (99%), cobalt (II) acetate tetrahydrate (99%) and nickel (II) acetate tetrahydrate (99%). Metal salts were dissolved in distilled water under stirring as per their hydrolysis constants (p^*K_1) in the following order: Sr^{2+} (13.8), La^{3+} (10.7), Mn^{2+} (10.6), Co^{2+} (9.7), and Ni^{2+} (9.4) for controlling the hydrolysis-condensation reactions [15]. This led to a clear solution (100 ml) of 0.3 M. Ethylene glycol ($C_2H_6O_2$, 99%, Aldrich; an esterification agent) and then citric acid ($C_6H_8O_7$, 99.5%, Aldrich; a chelating agent), both with mass equals to the total mass of cations available, were added drop-wise under stirring. The solution was continuously stirred at ~80 °C to obtain polymeric resin. The resin was dried at ~150 °C for 8 h to remove the solvent. It was then pre-calcined at ~450 °C for 1 h to burn out organic components and finally calcined at ~1100 °C for 2 h to produce ceramic oxide in powder form.

A solid electrolyte, namely YSZ (TG-8Y, BET surface area (S) 14 $m^2\,g^{-1}$, Tosoh, Japan), ScSZ (10Sc1CeSZ, $S \sim 14\,m^2\,g^{-1}$, Daichi Kigenso Kagaku Kogyo, Japan) or CGO ($S \sim 10$–$14\,m^2\,g^{-1}$, Rhodia, USA) was thoroughly mixed with the cathode powder in an equal weight proportion to form a composite. The composite was then sintered at ~1100 °C for 48 h for the reactivity study. Powder samples were pressed at ~392 MPa to form pellets of diameter ~11 mm and thickness ~1 mm for morphology and electrical property studies. Rectangular bars of dimension, ~5 mm × 5 mm × 20 mm, were prepared for thermal expansion behavior. The pellets and bars were sintered at ~1100 °C for 2 h in air.

A Rigaku X-ray diffractometer (D/Max, Japan) was used to record a diffractogram in a range of 20–80° with a step of 0.01° and a scan speed of 2° min^{-1}. A Rietveld analysis program, *MAUD* [16], was then applied for structural analysis using the full-profile fitting method. A program *Diamond* [17] was used to calculate bond lengths and bond angle. The crystallite size (D) was calculated at $2\theta \sim 46.8°$ (the highest single peak of the perovskite phase with rhombohedral symmetry) using the Scherrer formula, $D = 0.94\lambda/\beta\cos(\theta)$, where λ is the wavelength of the X-ray source (1.54056 Å) and β is the full width at half maxima. A Micromeritics pycnometer (Accupye 1330, USA) was used for measuring the density (ρ_m) of the powder sample. FT-IR spectra of the powder samples (in the KBr pellets) were recorded from 370–1000 cm^{-1} by a Bruker Fourier-transform infrared spectrometer (TENSOR 27, Germany, resolution 2 cm^{-1}) equipped with a KBr beam splitter. Differential thermal analysis-thermo-gravimetry (DTA-TG) was carried on the powder sample at a rate of 5 °C min^{-1} by a Setaram TG-DTA unit (TGA-92, France). Thermal expansion was recorded using a MAC Science dilatometer (TD5000S, Japan) at a rate of 10 °C min^{-1} and subsequently the coefficient of thermal expansion (α) was evaluated from the slope. A Hitachi scanning electron microscope (S-4200, Japan) was used for the morphology study. The BET surface area of powder was determined using a Micromeritics ASAP 2010 surface area analyzer (USA).

Electrical conductivity of a sintered pellet was measured using the van der Pauw four probe dc method. Contact points of platinum (Pt) on the pellet were made using the ion sputtering method. A silver paste was applied between Pt contact and Pt wire and subsequently heated to ~970 °C to ensure proper contact. A constant dc current of 1 mA was applied using a Keithley 224 current source meter and resulted voltage drop was measured by an Iwatsu digital meter (SC-7401, Japan). Ionic conductivity of a pellet was determined from the bulk resistance, an intercept at the real axis of Z'–Z'' complex plot recorded from 1 MHz to 1 kHz using a HP 4284A impedance analyzer. Platinum coated by the ion sputtering method was used as a blocking electrode. All experiments were performed in air.

3. Results and discussion

3.1. Phase evolution

Fig. 1 shows DTA-TG curves of dried polymeric gel for $La_{0.75}Sr_{0.25}Mn_{0.85}Co_{0.1}Ni_{0.05}O_{3+\delta}$ indicating evolution of perovskite phase with increasing temperature. The curves are similar to those of sol–gel derived LSM ($x = 0.3$ [18] or 0.15 [19]), which were explained using the mass and FT-IR spectroscopies. Thus, the observed endothermic and exothermic peaks along with the weight losses for $La_{0.75}Sr_{0.25}Mn_{0.85}Co_{0.1}Ni_{0.05}O_{3+\delta}$ can be explained as follows. A small and broad endothermic peak at ~150 °C, marked by A and accompanied by a weight loss of ~3% is a consequence of the loss of the residual adsorbed and hydrated water. Some prominent exothermic peaks at ~293, ~380 and ~597 °C, marked by B, C and D, respectively, and associated with a huge weight loss of ~34% are due to the decomposition-oxidation of the metal chelates and the evolved gases, and reaction of the decomposed chelates. Exothermic peaks, E and F appeared at ~675 and ~860 °C, respectively, are most probably due to formation of a phase as no significant weight loss is observed after ~900 °C.

Fig. 2 shows XRD patterns of the dried, pre-calcined and calcined samples of $La_{0.75}Sr_{0.25}Mn_{0.85}Co_{0.1}Ni_{0.05}O_{3+\delta}$. An amorphous nature is noticed for dried and pre-calcined samples probably due to presence of an intermediate oxyhydroxy carbonate phase [18]. A perovskite phase is developed at ~700 °C and identical to the rhombohedral $LaMnO_{3+\delta}$ (space group R – 3c, 167; $a = b = 5.6109(5)$, $c = 13.619(1)$ Å; number of formula units in the unit cell, $Z = 6$; unit cell volume, $V = 371.31$ $Å^3$; $\rho_{th} = 6.49\,g\,cm^{-3}$; JCPDS 85-2219). The rhombohedral nature was distinguished by a doublet of the main perovskite peak in the 2θ region, 32.3–32.8°, which is more favorable for a perovskite of form $A^{3+}B^{3+}O_3$ with larger A ions and smaller B ions [4]. A further increase in calcination temperature to ~1100 °C improves the rhombohedral symmetry as obvious by a splitting

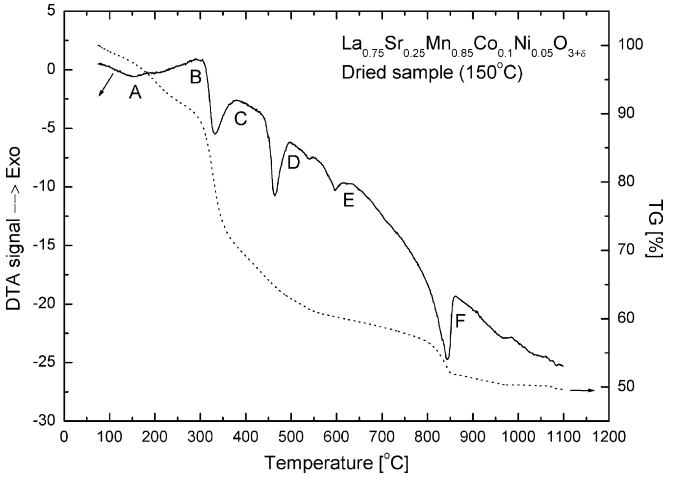

Fig. 1. DTA-TG curves of $La_{0.75}Sr_{0.25}Mn_{0.85}Co_{0.1}Ni_{0.05}O_{3+\delta}$.

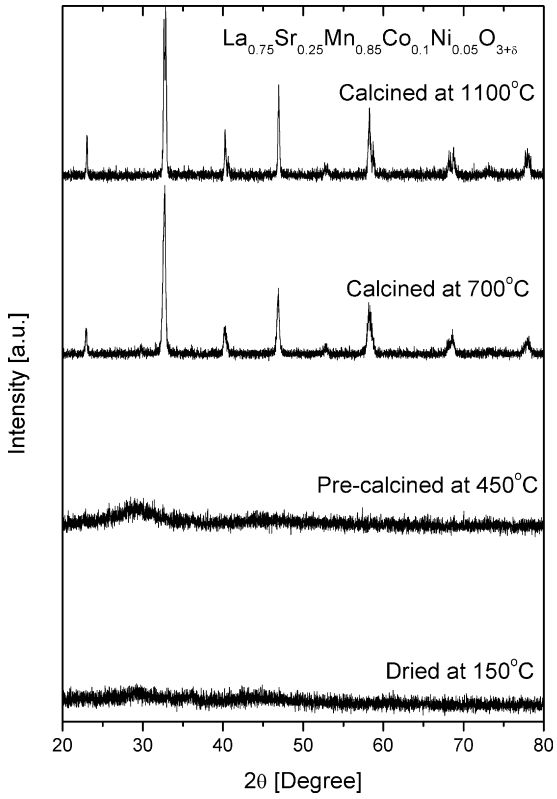

Fig. 2. XRD patterns of $La_{0.75}Sr_{0.25}$ $Mn_{0.85}Co_{0.1}Ni_{0.05}O_{3+\delta}$ dried at 150 °C, pre-calcined at 450 °C, calcined at 700 °C, and calcined at 1100 °C.

in the hexagonal reflection peaks and an increase in intensities of hexagonal peaks relative to the main peak.

3.2. Structure

Fig. 3 shows X-ray diffractograms of $La_{0.75}Sr_{0.25}$ $Mn_{0.95-x}Co_xNi_{0.05}O_{3+\delta}$ $(0.1 \le x \le 0.3)$. An X-ray diffractogram of $La_{0.75}Sr_{0.25}$ $MnO_{3+\delta}$ prepared identically is also included for a direct comparison. Despite of co-doping at the Mn-site with various concentrations, the rhombohedral nature of LSM is retained [18–21]. The XRD pattern is also found similar to that for $La_{0.7}Sr_{0.3}$

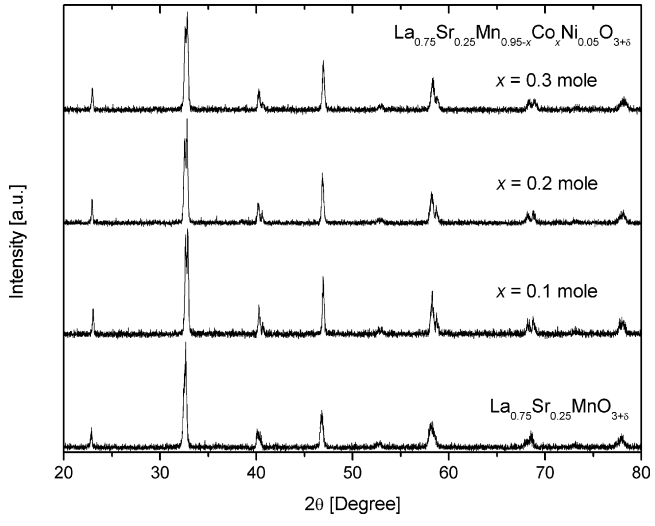

Fig. 3. X-ray diffractograms of $La_{0.75}Sr_{0.25}$ $Mn_{0.95-x}Co_xNi_{0.05}O_{3+\delta}$ (x = 0.1–0.3 mol) and $La_{0.75}Sr_{0.25}$ $MnO_{3+\delta}$.

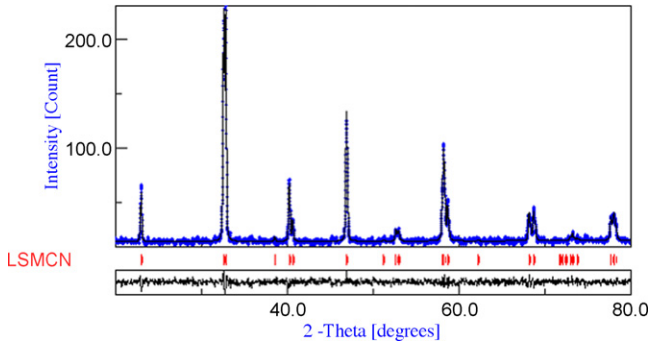

Fig. 4. Rietveld refined profiles of $La_{0.75}Sr_{0.25}$ $Mn_{0.85}Co_{0.1}Ni_{0.05}O_{3+\delta}$. The solid line is the calculated intensity and the plus is the observed intensity (the background was not subtracted). The short vertical lines show the possible Bragg reflections. The bottom corresponds to the difference between the observed and calculated intensities.

$Co_{1-z}Mn_zO_{3\pm\delta}$ $(0 \le z \le 1)$ [22]. In order to determine crystallographic parameters of $La_{0.75}Sr_{0.25}$ $Mn_{0.95-x}Co_xNi_{0.05}O_{3+\delta}$, the XRD data were refined using the *MAUD*. The Wyckoff positions used for the atoms of rhombohedral $La_{0.75}Sr_{0.25}$ $Mn_{0.95-x}Co_xNi_{0.05}O_{3+\delta}$, are La/Sr (6a: 0, 0, 0.25), Mn/Co/Ni (6b: 0, 0, 0) and O (18e: ~0.450, 0, 0.25) [22]. The (La/Sr)- and (Mn/Co/Ni)-sites occupancies were maintained at fixed values consistent with the nominal stoichiometry. Fig. 4 shows a typical Rietveld plot for the sample with x = 0.1 mole. The observed and calculated intensity profiles are well matched, which is obvious by their difference as shown in the bottom of the figure. The values of refinement parameters, R_{exp} and R_b, as shown in Table 1, are also close to each other indicating good quality of the profile fittings. The structural parameters of $La_{0.75}Sr_{0.25}$ $Mn_{0.95-x}Co_xNi_{0.05}O_{3+\delta}$ $(0.1 \le x \le 0.3)$ along with those of the rhombohedral $LaMnO_{3+\delta}$ [21] are shown in the Table 1 for direct comparison. For the sample with x = 0.1 mol, lattice constant a is low and c is high as compared to those of pure $LaMnO_3$, resulting in a decreased unit cell volume. An increase in x reduces the volume linearly due to a linear decrease in lattice constants. Consequently, this increases the theoretical density linearly. The measured density is noted almost invariant with increasing x, therefore relative density is almost same for all values of x. These observations are similar to those observed for LSCF [4] and Co^{2+}-doped LSM [10,22]. The compositional variation of V can be explained in the light of the defect models [23,24], as discussed below.

The pure and Sr^{2+} doped $LaMnO_{3+\delta}$ are well known for its apparent oxygen excess at the oxidizing conditions [23,24]. According to the defect models [23,24], pure $LaMnO_{3+\delta}$ changes into $La^{3+}{}_{1-y}$ $Mn^{3+}{}_{1-y}$ $Mn^{4+}{}_{1-y}$ O_3 for maintaining charge neutrality. This can be written in the Kroger–Vink notation as [23],

$$2La_{La}^{z} + 2Mn_{Mn}^{z} + 6O_{O}^{z} + \tfrac{1}{2}O_2(\text{gas}) \rightarrow \tfrac{2}{3}La_{La}^{z} + \tfrac{1}{3}V_{La}''' + Mn_{Mn}^{\bullet} + 3O_{O}^{z} + \tfrac{4}{3}La_{La}^{z} + Mn_{Mn}^{\bullet} + \tfrac{1}{3}V_{Mn}''' + 4O_{O}^{z}. \quad (1)$$

The lower index signifies the La-, Mn- and O-sites. The upper index indicates the charge compared to the normal charge of the $LaMnO_{3+\delta}$ without defects showing that (z) is neutral, ($'$) is −1 and ($^\bullet$) is +1. Thus, Mn_{Mn}^{z} and $Mn_{Mn}^{\bullet}$ denote Mn^{3+} and Mn^{4+} sitting on Mn-sites with a net charge of zero and +1, respectively. O_O^z denotes O^{2-} ions on oxygen sites with zero net charge. The Sr^{2+} substitution in La-site leads to a charge deficiency compensated in part by the oxidation of Mn^{3+} to Mn^{4+} and in part by the formation of oxygen vacancies ($V_O^{\bullet\bullet}$), that is,

$$Sr_{La}' = Mn_{Mn}^{\bullet} + 2V_O^{\bullet\bullet}. \quad (2)$$

Table 1
Lattice constants (a and c), unit cell volume (V), theoretical density (ρ_{th}), measured density (ρ_m), relative density (ρ), bond lengths (La–O and Mn–O), tilt angle (ω), refinement parameters (R_{exp} and R_b) and crystallite size (D) of $La_{0.75}Sr_{0.25}$ $Mn_{0.95-x}$ $Co_xNi_{0.05}O_{3+\delta}$ ($0.1 \le x \le 0.3$) and rhombohedral $LaMnO_3$. Number in parenthesis is statistical error of the last significant digit. The V′ is cell volume calculated from the Radaelli equation.

Parameters	$LaMnO_3$	$La_{0.75}Sr_{0.25}$ $Mn_{0.95-x}Co_xNi_{0.05}O_{3+\delta}$		
		$x = 0.1$	$x = 0.2$	$x = 0.3$
a (Å)	5.5280(1)	5.5066(1)	5.49910(9)	5.48945(8)
c (Å)	13.3404(3)	13.3481(5)	13.3225(3)	13.3051(5)
V (Å^3)	353.05	350.52(2)	348.90(1)	347.22(1)
V' (Å^3)	–	350.54	348.93	347.27
ρ_{th} (g cm^{-3})		6.53	6.57	6.61
ρ_m (g cm^{-3})	–	5.90	5.90	5.89
ρ	–	0.90	0.90	0.89
La–O(1) (Å) 3×	2.496(5)	2.5000(55)	2.5021(27)	2.5032(55)
La–O(2) (Å) 6×	2.750(2)	2.7460(25)	2.7407(25)	2.7362(25)
La–O(3) (Å) 3×	3.032(3)	3.0066(55)	2.9970(27)	2.9863(27)
⟨La–O⟩	2.757	2.750	2.745	2.740
Mn–O (Å) 6×	1.963(3)	1.9566(7)	1.9529(7)	1.9491(7)
ω (°)	9.89	7.44	7.28	7.12
R_{exp} (%)	–	20.6	18.98	18.15
R_b (%)	–	7.55	6.54	6.06
D (nm)	–	26	24	23

For a low Sr^{2+} content and at a reduced temperature, Mn^{4+} dominates, while at a high Sr^{2+} content and sufficiently high temperatures the oxygen vacancies dominate.

Mizusaki et al. [24] assumed vacancy excluding spaces (VES) around the metal vacancies and Sr'_{La}. The volume of VES around the metal vacancy was equal to 9 unit cells of the pseudo-cubic perovskite-type LSM, and that around Sr'_{La} to 3 unit cells. The defect equilibrium was expressed as,

$$\frac{3}{2}O_2(gas) + La^z_{La} \rightarrow LaMnO_3 + 2V'''_{La} + La^z_{Mn} + 6\dot{h}^*, \quad (3)$$

where La^z_{La} was considered to be outside the VES. The $\dot{h}^*$ is a hole which stays on the nonbonding oxygen level formed by La-site vacancies. It is either itinerant or trapped randomly throughout the crystal and different from the p-type carrier contributing the p-type conduction. The $\dot{h}^*$ was dependent on the number of metal vacancy rather than the Sr^{2+} content and mean Mn valence. They also showed a charge disproportion in Mn^{2+}, Mn^{3+} and Mn^{4+}. Tai et al. [4] proposed charge disproportion, ionic compensation and preferential electronic compensation mechanisms to explain the structural, thermal, and electrical properties of LSCF. According to them, trivalent cations (M^{3+}, M = Co or Fe) transform to the high and low valence cations as, $2M^{3+} \Leftrightarrow M^{2+} + M^{4+}$, which is a reversible process. Similarly, two M^{4+} ions can form M^{3+} ions. The concentration of M^{2+}, M^{3+}, and M^{4+} was also found dependent on the Sr^{2+} content and ambient temperature. An electro-neutrality condition similar to Eq. (2) was considered for the ionic compensation phenomenon. A transformation from Fe^{3+} to Fe^{4+} was noted more preferential than Co^{3+} to Co^{4+}. Huang et al. [5] suggested a charge transfer mechanism, $M^{3+} + Ni^{3+} \Leftrightarrow Ni^{2+} + M^{4+}$ for LSCN. Carter et al. [9] put forward an electro-neutrality condition similar to Eq. (2) for co-doped LSM. Thus, the volume contraction for $La_{0.75}Sr_{0.25}$ $Mn_{0.95-x}$ $Co_xNi_{0.05}O_{3+\delta}$ with increasing x is due to the transformation of trivalent cations of large ionic radii (Mn, 0.64 Å; Co, 0.61 Å; and Ni, 0.6 Å) to tetravalent cations of small ionic radii (Mn, 0.53 Å; Co, 0.53 Å; and Ni, 0.48 Å) along with a small fraction of divalent cations (Mn, 0.83 Å; Co, 0.74 Å; and Ni, 0.69 Å) [25].

The composition dependent V study is also corroborative to the bond lengths, La–O and Mn–O studies. Table 1 depicts the bonds lengths of $La_{0.75}Sr_{0.25}$ $Mn_{0.95-x}Co_xNi_{0.05}O_{3+\delta}$ ($0.1 \le x \le 0.3$) and rhombohedral $LaMnO_{3+\delta}$ [21]. The La–O(1) of $La_{0.75}Sr_{0.25}$ $Mn_{0.95-x}$ $Co_xNi_{0.05}O_{3+\delta}$ for all values of x is found slightly higher than that of $LaMnO_3$. However, La–O(2), La–O(3), average La–O (⟨La–O⟩) and Mn–O of samples with $x = 0.1$ mol are lower than those of $LaMnO_3$. An increase in x decreases the value of La–O(2), La–O(3), ⟨La–O⟩ and Mn–O linearly consequently decreasing the volume. This suggests that the co-doping decreases the mean ionic radius of Mn-site. However, owing to a large ionic radius of Sr^{2+} (1.44 Å) relative to that of La^{3+} (1.36 Å), the La–O(1) is higher than that of $LaMnO_3$ [25].

Radaelli et al. have been shown using an expression, $V' \approx Z(2Mn - O\cos\omega)^3$ that the unit cell volume, V' is directly proportional to the Mn–O and tilt angle (ω) [26]. The ω also represents the distortion of the MnO_6 octahedra with respect to the cubic phase ($\omega = 0°$) [21]. The tilt angle is therefore calculated using an expression, $\omega = (180° - \theta_{Mn-O-Mn})/2$, where $\theta_{Mn-O-Mn}$ is the bond angle. Subsequently, V' is computed for $La_{0.75}Sr_{0.25}$ $Mn_{0.95-x}$ $Co_xNi_{0.05}O_{3+\delta}$ ($0.1 \le x \le 0.3$) and presented in Table 1. The compositional variations of ω and V' are found identical to the V–x variation. A linear decrease in ω is also noted with increasing x suggesting a decrease in structural distortion. The crystallite size (D) is also decreased linearly with increasing x well supporting the bond lengths versus x study. The V–x study is further supported by the spectroscopy study, which has been discussed below.

A change in volume of $LaMnO_3$ perovskite is associated to the deformation of LaO_{12} and MnO_6 polyhedra via variations of their bond lengths and bond/tilt angle [26–30]. The Mn–O was found inversely proportional to the high-frequency stretching mode and the La–O was proportional to the bending mode. Hence, in order to correlate the observed bond-lengths with the stretching and bending modes, the infrared spectroscopy study is carried out for $La_{0.75}Sr_{0.25}$ $Mn_{0.95-x}$ $Co_xNi_{0.05}O_{3+\delta}$ ($x = 0.1$–0.3 mol) and presented in Fig. 5. The FT-IR spectra of $La_{0.75}Sr_{0.25}$ $Mn_{0.95-x}Co_xNi_{0.05}O_{3+\delta}$ are similar to those of rhombohedral perovskites: pure [27–29] and doped $LaMnO_{3+\delta}$ [30]. Therefore, an irreducible representation for the optical mode can be represented as: $\Gamma_{opt} = \Gamma_{Raman} + \Gamma_{IR} + \Gamma_{Inactive} + \Gamma_{Acoustic}$. $\Gamma_{Raman} = A_{1g} + 4E_g$ corresponds to Raman active modes. Γ_{IR}, $= 3A_{2u} + 5E_u$ indicates IR active modes. $\Gamma_{Inactive}$ ($= 2A_{1u} + 3A_{2g}$) and $\Gamma_{Acoustic}$ ($= A_{2u} + E_u$) are acoustic and inactive modes, respectively. Similarly, the site symmetry can be represented as, La/Sr (D_3), Mn/Co/Ni (C_{3i}), and O (C_2). Thus, eight IR active modes can be available for $La_{0.75}Sr_{0.25}$ $Mn_{0.95-x}Co_xNi_{0.05}O_{3+\delta}$. The observed vibrational bands and possible assignments of $La_{0.75}Sr_{0.25}$ $Mn_{0.95-x}Co_xNi_{0.05}O_{3+\delta}$ with respect to rhombohedral $LaMnO_3$ are shown in Table 2. Some noteworthy

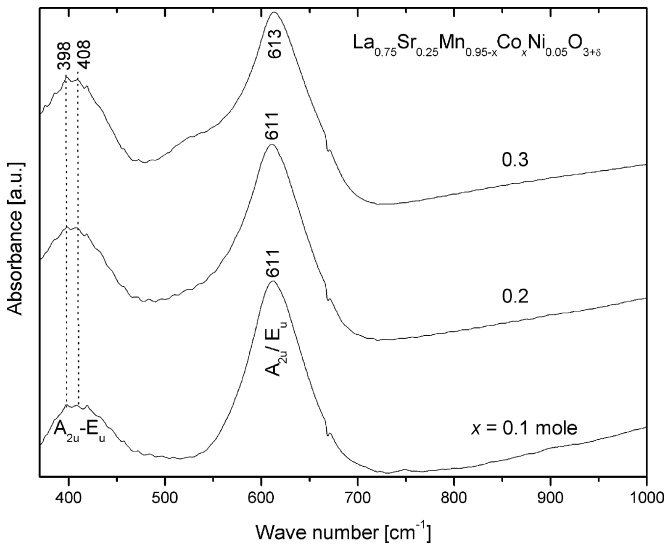

Fig. 5. FT-IR spectra of $La_{0.75}Sr_{0.25}$ $Mn_{0.95-x}Co_xNi_{0.05}O_{3+\delta}$ ($0.1 \le x \le 0.3$).

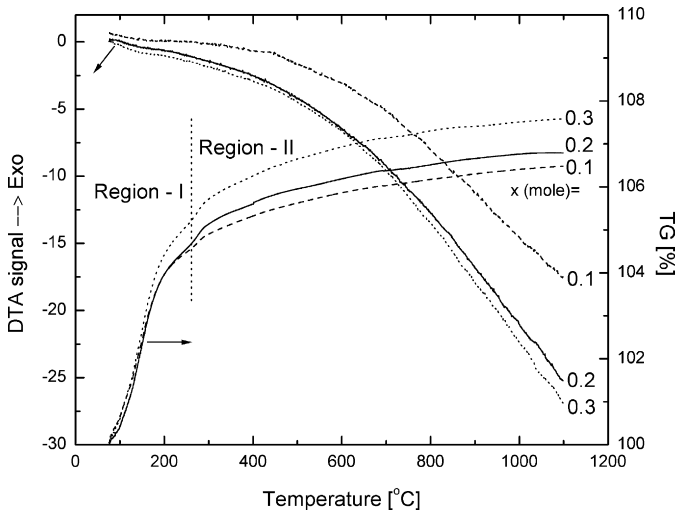

Fig. 6. DTA-TG curves of $La_{0.75}Sr_{0.25}$ $Mn_{0.95-x}Co_xNi_{0.05}O_{3+\delta}$ ($0.1 \le x \le 0.3$).

features observed with increasing x, and related to the bond lengths are as follows.

(i) The peak position of high frequency stretching E_u–A_{2u} mode pair for $La_{0.75}Sr_{0.25}$ $Mn_{0.85}Co_{0.1}$ $Ni_{0.05}O_{3+\delta}$ is higher than that of pure $LaMnO_3$. The wave number of stretching mode pair is remained invariant for $x = 0.1$ and 0.2 mole and slightly up-shifted for $x = 0.3$ mol. This indicates a decrease in Mn–O and hence a decrease in cell volume, as observed earlier.

(ii) A split in peak position of the mid frequency bending E_u–A_{2u} mode pair is noticed. It is probably due to a large lattice distortion by Sr^{2+} having a larger ionic radius than La^{3+} as observed by the La–O(1) bond length study and also predicted by Mizusaki et al. [24,30].

3.3. Thermal properties

The oxygen stoichiometry ($3+\delta$) of a perovskite system is determined qualitatively by TG [4]. For LSM, oxygen non-stoichiometry (δ) was decreased with increasing temperature and x, and decreasing oxygen partial pressure [18,23,24]. The defect reaction can be expressed with increasing temperature as $4Mn^{z}_{Mn} + 4e^{-} \rightarrow 4Mn'_{Mn}$ by increasing the oxygen vacancies via $2O^{z}_{O} \rightarrow 2V_{O}^{\bullet\bullet} + O_2(gas) + 4e^{-}$ [24]. The oxygen atom removed from the lattice, left a net positive charge of 2+. The value of δ was calculated to be zero for Sr^{2+} concentration greater than 0.329 mol [24]. Mori et al. [31] observed a linear volume expansion with increasing temperature for LSM. For LSCF, a decrease in oxygen stoichiometry was accompanied with an increase in the thermal expansion and the seebeck coefficient, and a decrease in the electronic conductivity [4]. An increase in the seebeck coefficient indicated a reduction in the carrier concentration and the site occupancy. The oxygen stoichiometry is therefore determined for $La_{0.75}Sr_{0.25}$ $Mn_{0.95-x}Co_xNi_{0.05}O_{3+\delta}$ ($x = 0.1$–0.3 mol) and shown in Fig. 6 along with the DTA curves. No exothermic and endothermic peaks are observed in the DTA curves suggesting a stabilization of rhombohedral phase for the temperature regime, 50–1100 °C. The TG is increased from 100 to ~105 in region I (25–260 °C), then to ~107 in region II (300–1100 °C), confirming the excess oxygen content of the system. This also indicates a large increase in oxygen vacancies in region I and its invariance in region II [9]. A change in slopes is observed in a temperature region 260–290 °C probably due to the Jahn–Teller structural transition as observed earlier for the nearly stoichiometric $LaMnO_{3+\delta}$ [32]. It is also worth mentioning that the TG increases with increasing x, suggesting an increase in oxygen vacancies. This provides easy pathways for oxygen ion motion as observed by ionic conductivity–temperature study discussed later. This also suggestes that the volume expansion with increasing temperature is the highest for $x = 0.3$ mole as observed by the thermal expansion study (Fig. 7). The thermal expansion increases linearly with increasing temperature in both the regions, I and II. As mentioned earlier, it is due to a gradual decrease in δ between the cations and the oxygen, and consequently an increase in oxygen vacancies. Owing to a large amount of oxygen vacancies, the region II possesses a slope higher than that in the region I. Moreover, the value of slope is increased with increasing x. Therefore, coefficient of thermal expansion computed from the slope of thermal expansion curve for region II and showed as an inset in Fig. 7, is the highest for $x = 0.3$ mol.

3.4. Morphology

Fig. 8 shows SEM micrographs for fractured surface of $La_{0.75}Sr_{0.25}$ $Mn_{0.95-x}Co_xNi_{0.05}O_{3+\delta}$ ($x = 0.1$–0.3 mol). Particles are found almost spherical for all values of x. The average particle size is calculated to be ~967, ~690 and ~530 nm for $x = 0.1$, 0.2 and 0.3 mol, respectively. The average size of particles is decreased with increasing x due to a decrease in crystallite size, which is in good agreement with the study reported by Kuharuangrong et al. [10] for Co^{2+}-doped

Table 2
Observed vibrational bands (in cm^{-1}) and possible assignments of $La_{0.75}Sr_{0.25}$ $Mn_{0.95-x}Co_xNi_{0.05}O_{3+\delta}$ with respect to those of rhombohedral $LaMnO_3$. Superscript, a–c corresponds to ref. [27–29], respectively. LDC, lattice dynamical calculated value.

Mode	$LaMnO_3$		$La_{0.75}Sr_{0.25}$ $Mn_{0.95-x}Co_xNi_{0.05}O_{3+\delta}$		
	LDC[a]	Exp.	$x = 0.1$	$x = 0.2$	$x = 0.3$
E_u–A_{2u} stretching	642	586[a], 608[b], 603[c]	611	611	613
E_u bending	357	395[a], 395[b], 405[c]	408	408	408
A_{2u} bending	357	395[a], 395[b], 405[c]	398	398	398

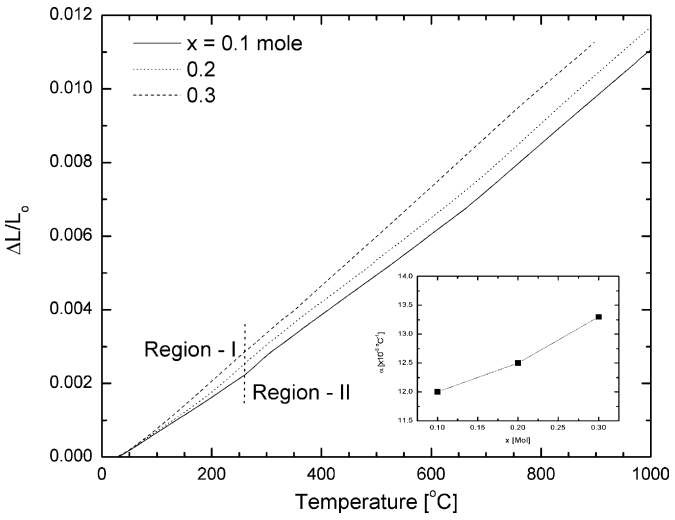

Fig. 7. Thermal expansion curves of $La_{0.75}Sr_{0.25}$ $Mn_{0.95-x}Co_xNi_{0.05}O_{3+\delta}$ ($0.1 \le x \le 0.3$). Inset, coefficient of thermal expansion (α) with x.

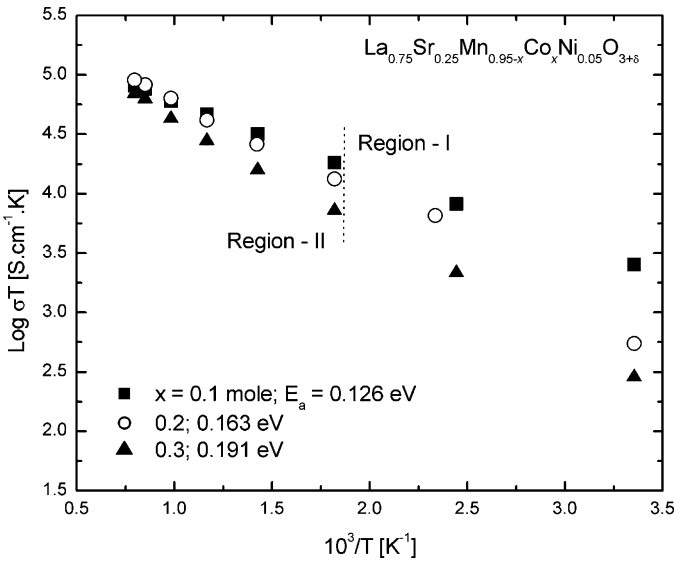

Fig. 9. Log σT versus $1/T$ plots for $La_{0.75}Sr_{0.25}$ $Mn_{0.95-x}Co_xNi_{0.05}O_{3+\delta}$ ($0.1 \le x \le 0.3$).

LSM. The average particle size (d) of powder is also calculated using an expression, $d = 6/\rho_{th} S$ [19]. The BET surface area (S) is determined to be ~1.26 $m^2\ g^{-1}$ for $x = 0.1$ mol resulting in average particle size ~730 nm, which is close to the value determined using the SEM.

3.5. Electrical properties

Fig. 9 shows temperature dependence of electrical conductivity (σ) of $La_{0.75}Sr_{0.25}Mn_{0.95-x}$ $Co_xNi_{0.05}O_{3+\delta}$ ($x = 0.1$–0.3 mol). The electrical conductivity is increased linearly with increasing temperature in region II and obeyed the relation, $\sigma = (\sigma_o/kT)\exp(-E_a/kT)$, for the adiabatic small polaron hopping mechanism as observed earlier for the pure [19,24] and doped [10,11] LSM. The notation, σ_o is a pre-exponential factor containing the terms such as the carrier concentration and the average distance between the Mn ions. The E_a is the activation energy for small-polaron conduction and other notations have their usual meanings. The values of σ for $x = 0.1$–0.3 mol are found close to each other at high temperatures most probably due to an influence of the $LaCoO_3$ [10]. At high temperature ~1000 °C, $La_{0.8}Sr_{0.2}CoO_3$ exhibits fairly high electronic conductivity (~1000 S cm^{-1} [4]) due to electrons as predominant charge carriers, while $La_{0.8}Sr_{0.2}MnO_3$ possesses high electronic conductivity (~190 S cm^{-1} [24]) due to holes. An increase in x decreases the electrical conductivity at ~600 °C. The E_a-value, calculated from the slope of the log $\sigma T - 1/T$ variation in the region II and shown in the Fig. 9, is increased with increasing x. The sample with $x = 0.1$ mol exhibits the optimal values of electrical conductivity ($\sigma_{600°C} \sim 55$ S cm^{-1}) and activation energy ($E_a \sim 0.13$ eV). The value of electrical conductivity for $x = 0.1$ mol is also found lower than that for the LSM with Sr^{2+} content = 0.2 mol ($\sigma_{600°C} \sim 180$ S cm^{-1} [24]). This can be explained on the basis of Mizusaki's defect model [24]. A co-doping of Co^{2+} and Ni^{2+} at the Mn-site of LSM forms extra cation vacancies. With the formation of cation vacancies, a nonbonding oxygen 2p level is formed by the oxide ions around the vacancies. The formed level is narrow and the mobility of electrons in this level is low. The conductive $e_g(\uparrow)$ level and the low mobility $t_{2g}(\downarrow)$ level of Mn are very close to each other and lower than the nonbonding level. This nonbonding level serves as a hole-trap reducing the electronic conductivity with increasing x. A reduction in the available sites of Mn^{3+} for hole hopping can also be attributed for a decrease in electrical conductivity of doped LSM [10,11].

The co-doping provides more oxygen vacancies for maintaining the charge neutrality by decreasing the electronic charge carriers [4,9]. As suggested by the temperature dependent TG study (Fig. 6), one may expect a large increase in ionic conductivity in region I and then almost invariance for region II. Fig. 10 shows ionic conductivity (σ_{ion}) versus temperature curves of $La_{0.75}Sr_{0.25}$ $Mn_{0.95-x}Co_xNi_{0.05}O_{3+\delta}$ for $x = 0.1$–0.3 mole. The trend of log σ_{ion} – 1/T variations supports well that of the TG – temperature curves. It is also obvious that an increase in x increases the ionic conductivity in the region II. This is probably due to a large increase in oxygen vacancies by relatively less redox stable Co ions as compared to the Mn ions [9]. Thus, one can expect a high catalytic activity for the sample with $x = 0.3$ mol possessing fairly high ionic

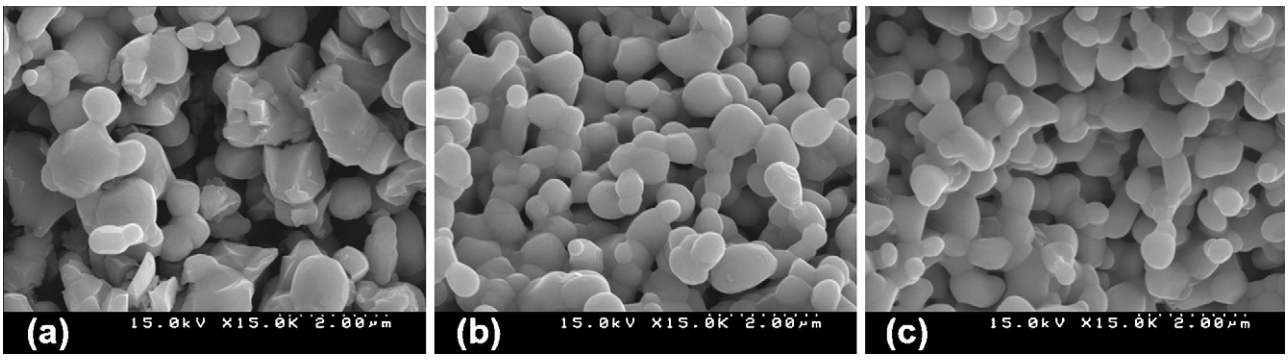

Fig. 8. SEM micrographs for fractured surface of $La_{0.75}Sr_{0.25}$ $Mn_{0.95-x}Co_xNi_{0.05}O_{3+\delta}$ ($0.1 \le x \le 0.3$). Bar, 2 μm.

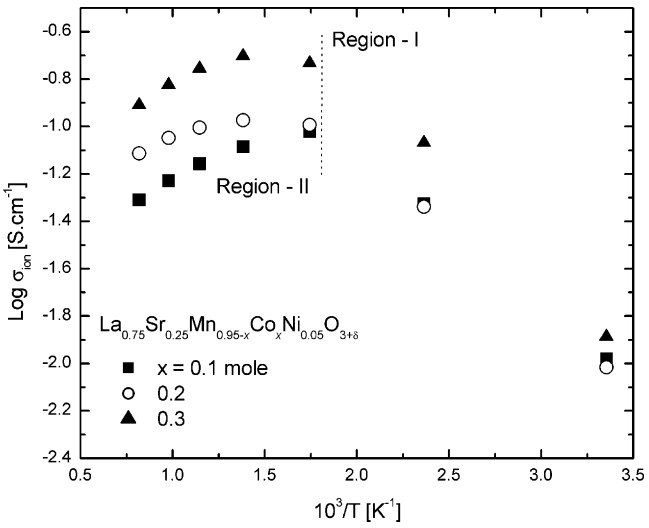

Fig. 10. Logarithm of ionic conductivity (σ_{ion}) versus $1/T$ plots for $La_{0.75}Sr_{0.25}Mn_{0.95-x}Co_xNi_{0.05}O_{3+\delta}$ ($0.1 \le x \le 0.3$).

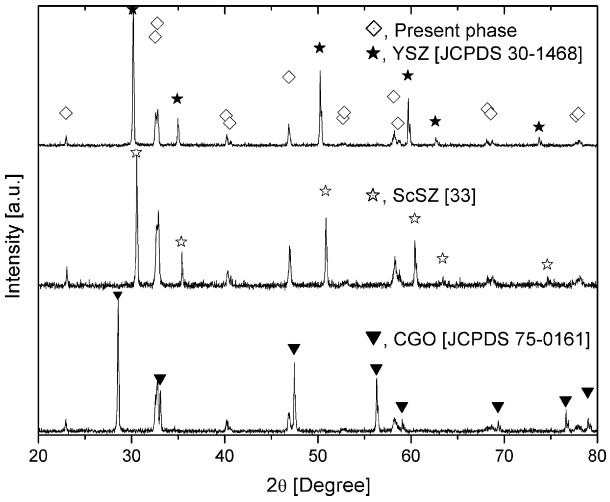

Fig. 11. XRD patterns of composites containing $La_{0.75}Sr_{0.25}Mn_{0.85}Co_{0.1}Ni_{0.05}O_{3+\delta}$ and an electrolyte, YSZ, ScSZ or CGO, and sintered at 1100 °C for 48 h.

conductivity in region II and comparable to that of LSCF [9]. The sample with $x = 0.1$ mole exhibits a sufficiently high ionic conductivity, $5–9 \times 10^{-2}$ S cm^{-1}, making it suitable as a cathode for IT-SOFC application.

3.6. Reactivity

Fig. 11 shows X-ray diffractograms of composites along with the reflection peaks of $La_{0.75}Sr_{0.25}Mn_{0.85}Co_{0.1}Ni_{0.05}O_{3+\delta}$, YSZ [JCPDS 30-1468], ScSZ [33] and CGO [JCPDS 75-0161] for direct comparison. The XRD patterns of the composites show no new reflection peaks apart from the reflection peaks of the constituent phases. This infers the absence of a secondary phase as a consequence of any reaction between the cathode and solid electrolyte.

4. Conclusions

A rhombohedral perovskite-type system, $La_{0.75}Sr_{0.25}Mn_{0.95-x}Co_xNi_{0.05}O_{3+\delta}$ with $x = 0.1–0.3$ mol, was synthesized using metal acetates by the Pechini method. A decrease in unit cell volume, bond lengths, tilt angle and crystallite/particle size was observed with increasing x, accompanying with an increase in wave number of stretching mode pair. The TG, coefficient of thermal expansion and ionic conductivity were increased, while electrical conductivity was decreased with increasing x. The samples with $x = 0.1$ mol exhibited electrical conductivity ~55 S cm^{-1} at 600 °C, activation energy ~0.13 eV, coefficient of thermal expansion $\sim 12 \times 10^6$ °C^{-1} and sufficiently high ionic conductivity $5–9 \times 10^{-2}$ S cm^{-1}, making it suitable as a cathode for IT-SOFC application. The reactivity between the cathode and solid electrolytes was found negligible.

Acknowledgements

Prof. Jung Hyun Kim, Department of Chemical Engineering, Yonsei University is thankfully acknowledged for providing the FT-IR spectroscopy facility. The authors are grateful to the BK21 Program and Seoul Technology Foundation of the Korean Government for the financial assistance.

References

[1] P. Holtappels, U. Stimming, in: W. Vielstich, H.A. Gasteiger, A. Lamm (Eds.), Handbook of Fuel Cells – Fundamentals, Technology and Applications, 1, John Wiley & Sons, Chichester, 2003, Ch 20.
[2] O. Yamamoto, in: W. Vielstich, H.A. Gasteiger, A. Lamm (Eds.), Handbook of Fuel Cells – Fundamentals, Technology and Applications, 4, John Wiley & Sons, Chichester, 2003, Chapter 71.
[3] B.C.H. Steele, A. Heinzel, Nature 414 (2001) 345–352.
[4] L.W. Tai, M.M. Nasrallah, H.U. Anderson, D.M. Sparlin, S.R. Sehlin, Solid State Ionics 76 (1995) 259–271.
[5] K. Huang, H.Y. Lee, J.B. Goodenough, J. Electrochem. Soc. 145 (1998) 3220–3227.
[6] S. Simner, M. Anderson, J. Bonnett, J. Stevenson, Solid State Ionics 175 (2004) 79–81.
[7] S. Wang, R. Zheng, A. Suzuki, T. Hashimoto, Solid State Ionics 174 (2004) 157–162.
[8] Z. Shao, S.M. Haile, Nature 431 (2004) 170–173.
[9] S. Carter, A. Selcuk, R.J. Chater, J. Kajda, J.A. Kilner, B.C.H. Steele, Solid State Ionics 53-56 (1992) 597–605.
[10] S. Kuharuangrong, T. Dechakupt, P. Aungkavattana, Mater. Lett. 58 (2004) 1964–1970.
[11] S. Kuharuangrong, Ceram. Int. 30 (2004) 273–277.
[12] K. Kakinuma, S. Machida, T. Arisaka, H. Yamamura, T. Atake, Solid State Ionics 176 (2005) 2405–2410.
[13] K. Kakinuma, S. Machida, K. Horiuchi, S. Hasunuma, H. Yamamura, T. Atake, Solid State Ionics 177 (2006) 2159–2164.
[14] M. Pechini, 1967, US Patent 3330697.
[15] J. Burgess, Metal Ions in Solution, John Wiley & Sons, NY, 1978, pp. 264–395.
[16] L. Lutterotti, MAUD, 2006, Version 2.044, Itali.
[17] K. Brandenburg, Diamond, 2008, Version 3.1e, Germany.
[18] M. Gaudon, C. Laberty-Robert, F. Ansart, P. Stevens, A. Rousset, Solid State Sci. 4 (2002) 125–133.
[19] C.N. Chervin, B.J. Clapsaddle, H.W. Chiu, A.E. Gash, J.H. Satcher Jr., S.M. Kauzlarich, Chem. Mater. 18 (2006) 1928–1937.
[20] A. Hammouche, E. Siebert, A. Hammou, Mater. Res. Bull. 24 (1989) 367–380.
[21] R. Millini, M.F. Gagliardi, G. Piro, J. Mater. Sci. 29 (1994) 4065–4069.
[22] A.N. Petrov, V.I. Voronin, T. Norby, P. Kofstad, J. Solid State Chem. 143 (1999) 52–57.
[23] A.N. Grundy, E. Povoden, T. Ivas, L.J. Gauckler, Comput. Coupling Phase Diagrams Thermochem. 30 (2006) 33–41.
[24] J. Mizusaki, N. Mori, H. Takai, Y. Yonemura, H. Minamiue, H. Tagawa, M. Dokiya, H. Inaba, K. Naraya, T. Sasamoto, T. Hashimoto, Solid State Ionics 129 (2000) 163–177;
J. Mizusaki, Y. Yonemura, H. Kamata, K. Ohyama, N. Mori, H. Takai, H. Tagawa, M. Dokiya, K. Naraya, T. Sasamoto, H. Inaba, T. Hashimoto, Solid State Ionics 132 (2000) 167–180.
[25] R.D. Shannon, Acta Cryst. A32 (1976) 751–767.
[26] P.G. Radaelli, G. Iannone, M. Marezio, H.Y. Hwang, S.W. Cheong, J.D. Jorgensen, D.N. Argyriou, Phys. Rev. B 56 (1997) 8265–8276.
[27] M.V. Abrashev, A.P. Litvinchuk, M.N. Iliev, R.L. Meng, V.N. Popov, V.G. Ivanov, R.A. Chakalov, C. Thomsen, Phys. Rev. B 59 (1999) 4146–4153.
[28] M. Daturi, G. Busca, R.J. Willey, Chem. Mater. 7 (1995) 2115–2126.
[29] C. Roy, R.C. Budhani, J. Appl. Phys. 85 (1999) 3124–3131.
[30] G. De Marzi, Z.V. Popovic, A. Cantarero, Z. Dohcevic-Mitrovic, N. Paunovic, J. Bok, F. Sapina, Phys. Rev. B 68 (2003) 064302.
[31] M. Mori, Y. Hiei, N.M. Sammes, G.A. Tompsett, J. Electrochem. Soc. 147 (2000) 1295–1302.
[32] R. Zenati, C. Bernard, C. Calmet, S. Guillemet, G. Fantozzi, B. Durand, J. Eur. Ceram. Soc. 25 (2005) 935–941.
[33] S. Sarat, N. Sammes, A. Smirnova, J. Power Sources 160 (2006) 892–896.